NuVinci drive: Modeling and performance analysis

NuVinci drive: modeling and performance analysis

Tomaselli M.[2], Bottiglione F.[1,*], Lino P.[2], Carbone G.[1]
[1] *Dipartimento di Meccanica Matematica e Management (DMMM), Via Orabona 4 - 70125 Bari and*
[2] *Dipartimento di Ingegneria Elettrica e dell'Informazione (DEI), Via Orabona 4 - 70125 Bari*

The continuous search for more efficient drives, recently motivated also by environmental issues and innovative electro-mechanical applications, has led to a renovated interest in Continuously Variable Transmissions (CVTs). Several novel geometries of traction drives have been proposed in the recent past, to improve the performance sometimes with a look at miniaturization. A modified version of the well-known Kopp variator has recently been engineered under the name of NuVinci drive. NuVinci was designed for being installed on bicycles but with the promise to be suitable also for a wide range of other applications. In this paper, we present a mathematical model of this device, developed to study its performance, compare different relevant variants and improve the design. The performances are discussed in terms of traction capabilities and efficiency. It is shown how a slight modification of the geometry may lead to an evident change of the performance indicators, in particular the efficiency.

I. INTRODUCTION

In recent years, the increasing need for energy saving and reduction of pollutant or greenhouse gas emissions has turned into an emergency. This has pushed engineering research to develop solutions for improving the efficiency of any type of energy-consuming device. In the world of mechanical drives, besides the development of new technologies for motors, it is common to assign this task to the mechanical transmissions. Mechanical transmissions act to adapt the motor characteristics (engines, electric drives, others) to the torque-velocity requirements of the load [1]. For an optimal exploitation of the given motor, the ideal transmission should be: light, small, easy to control, lossless and able to make the whole powertrain work at its optimal efficiency, for any power request. Of course, in real applications, the adaptation is not optimally reached, and a tradeoff must be found.

Until recent years, simplicity of the transmissions has been preferred to the functional optimization of the drive as a whole, thus tolerating that motors work even far from their best efficiency points. However, the search for stronger optimality is now such a pressing need that a considerable amount of research work is dedicated even to more complicated transmissions schemes, aiming at reducing the operational costs and the environmental impact of the drive.

The matching between motor and load is achieved through the speed ratio of the transmission. Speed ratio can be constant or variable. In the latter case, it can be varied by steps or seamlessly between the minimum and maximum extremes. Under a purely functional point of view, the most effective transmissions enable a seamless variation of the speed ratio and over a wide range of values. Such transmissions are commonly named Continuously Variable Transmissions (CVT) or Infinitely Variable Transmissions (IVT), the last being those comprising the neutral gear (speed ratio equal to zero) in the range of allowed speed ratios. The main limitations of CVT and IVT are the efficiency and the management of speed ratio control.

Mechanical CVTs can be developed in several ways [2]. The most widespread classes are the belt/chain CVTs [3] and the traction drives [4, 5], all based on the transmission of torque by tangential contact forces.

Belt and chain CVTs have been studied extensively. Their behavior in steady-state [6–8] and ratio-shifting [9–11] operating conditions have been well understood. They are commonly characterized by the fact that ratio control needs the application of quite large forces. Indeed, for relatively large power applications like in the automotive field, clamping and shifting are achieved by means of a hydraulic circuit. Transmission layout may lead to some difficulties because of the relatively large wheelbase. They are widely and successfully employed in automotive applications (almost all CVT-equipped vehicles have a belt or a chain CVT). The main power losses are velocity losses due to the sliding contact of pulleys and belt, shifting losses due to the radial sliding, power consumption of the clamping and shifting mechanism and, in the case of a rubber belt, the hysteresis of the belt.

Toroidal drives differ for the shape of the toroidal cavities, the number and the shape of rollers. The basic schemes are the full-toroidal and the half-toroidal drives with almost cylindrical rollers. The half-toroidal architecture has been also employed in the automotive field up to fifteen years ago, (e.g. Nissan Extroid transmission, developed for high torque engines).

Full and half toroidal drives are very similar in principle but very differ considerably in the way they control the speed ratio [12–15]. In the former case, larger forces are needed to control the ratio. The main power losses are due to the local sliding at the contact between rollers and discs with the toroidal cavity. The local sliding is a combination of gross creep, spin, and sideslip. Creep is a measure of the local sliding in the direction of the traction forces. Spin is a measure of the local sliding due to the component of the relative angular velocity between contacting bodies perpendicular to the surfaces in contact [16]. Sideslip is a measure of the local sliding in the direction perpendicular to traction forces. All these phenomena involve power losses, but while creep is proportional to the torque transferred, spin is passively related to the contact force (thus the clamping force). The side-slip is related to the ratio shifting so its effect is limited to dynamic (ratio shifting) conditions [17]. It has been demonstrated that half-toroidal is better in terms of efficiency than the full-toroidal because spin losses are smaller on average [18]. Half and full toroidal drives have also been compared under dynamic working conditions [19] by incorporating the tribological model developed in [18] in a dynamic rigid body model of the drives.

Spin is the primary cause of reduction of the traction drive efficiency. For this reason, to limit the spin losses, several innovative geometries have been proposed and are currently under investigation, like the double-roller full-toroidal variator (DFTV) [20, 21] and the logarithmic toroidal drive [22]. Also, optimization algorithm of recent generation has been applied to optimize conventional half-toroidal drive geometry [23].

The ball CVT traction drives are similar to toroidal drives. Among them, the Kopp variator is maybe the eldest and the most widely used in industrial applications due to its robustness. It consists of a couple of discs with an almost cylindrical outer surface in contact with ball drives, whose rotational axis can be tilted to change the speed ratio. Discs are in contact with balls on their outer radii, thus the balls are set outside the discs and held in place by an outer idle ring. Performance of ball CVT has been evaluated by following the approach developed in [18] and compared to an half-toroidal CVT working in same conditions [24]. It was found therein that the efficiency of ball

(Kopp-type) variator can be smaller or larger than the half-toroidal efficiency depending on the value of the driven torque.

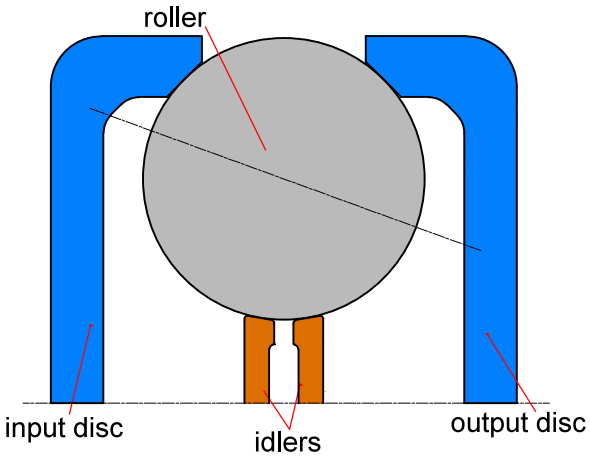

Figure 1. Main parts of a NuVinci CVT.

Fallbrook (Motion Technologies LLC before 2004) has developed a similar drive [25], presently known as NuVinci CVT. NuVinci was originally developed for bicycles, and later proposed also for cars under the name of VariGlide [26], for assisted e-bikes, variable speed wind turbines and other applications. The main components of NuVinci are shown in Figure 1. The input and output discs have narrow faces in contact with the ball elements. The rollers are spherical (balls). The ball rollers are held in contact with two central elements named idlers (one in the original patent [27–29]) as it appears disassembling a transmission bought in 2017, which are free to rotate. Tilting the rotational axles of the balls controls speed ratio. This is accomplished through the longitudinal movement of the idlers or equivalent mechanisms depending on the specific patent of the same company. The stator prevents the ball elements from rotating around the CVT's primary longitudinal axis by constraining movement of the ball axle ends. Typically the efficiency of the ball drives (Kopp, NuVinci) is in the range of 70% to 89% [2]. However, NuVinci geometry differs significantly from the Kopp type because the NuVinci's traction contacts are set on the inside diameter of discs thus on the outer edge of the ball variator. For a given radial encumbrance and torque transfer, the traction forces on discs and rollers are smaller because contacts are farther from the main longitudinal axis. This means that for a given torque requirement, the necessary clamping force is smaller in NuVinci. Since the mechanical losses are strictly related to the clamping force, this geometry is effective for improving the efficiency of ball drives. From another perspective, given the maximum tolerable clamping force, NuVinci torque capacity is larger than Kopp drive.

NuVinci architecture has some advantages if compared to other existing CVT technologies. Quoting [30] unlike the shift mechanisms for all other traction type CVTs, NuVinci CVT's shift mechanism is packaged internally, and it only carries small shift forces. This is possible because the rolling elements form a closed force couple, thus isolating the shift mechanism from clamp force components. Moreover, the shift mechanism also does not have to handle high spin forces, or forces induced by "steering" to a new ratio. Since the speed ratio control system is one of the most critical components of the commonly adopted CVTs (half and full toroidal types), this is the first reason why it is important to determine the performance indicators of NuVinci CVT.

A second fundamental reason is that the NuVinci CVT can be easily converted to CVP (Continuously Variable Planetary) which is a sort of planetary gear train with variable gear ratio. This operation mode is obtained by releasing the carrier (before mentioned as stator) of the tilting roller balls and connecting it to a third usable shaft. If all the shafts are left movable, then it can be used as a differential/combinatorial transmission, which can be suitably used for hybrid vehicles. A second possibility is to keep one of the two discs stationary, thus obtaining a planetary single-in single-out CVT with a different speed range compared to the original CVT. NuVinci, as a planetary CVT, enables to change the wise of rotation of the output for one given input (as a compact power-split Infinitely Variable Transmission or IVT), making the NuVinci almost unique in the CVT panorama. Very recently, researchers have presented the idea to convert also half-toroidal CVT to a compact power-split transmissions [31]. However, technical issues have yet to be solved for a practical application, whilst the NuVinci is already on the market and ready to be used. This characteristic opens the CVT world also to non-conventional applications like wearable robots or prosthetic devices [32] where packaging is such a strict requirement, that novel and specific CVTs [33] and planetary CVTs [34–36] have been studied recently.

In this paper, a mathematical model of NuVinci CVT mechanics briefly presented in [37] is extensively employed for

studying in details the kinematics, the traction performance and the efficiency. Section II describes the model. The geometry of the most recent variant of the variator (hereafter double-idler architecture) is described, then the kinematic quantities and characteristics are given. The relevant equilibrium equations are also presented in a convenient non-dimensional form; the efficiency is defined and discussed. The fundamental tribological model, which is adapted from ref. [18], is cited and conveniently reported in the Appendix A. An identical approach is applied to a different architecture, here indicated as single-idler, which is the one of the first patent. Then, for given size of the variator, simulations results are shown and discussed in sec. III, comparing the performance of the double-idler and single-idler geometries.

II. VARIATOR MODEL

A. Geometrical description

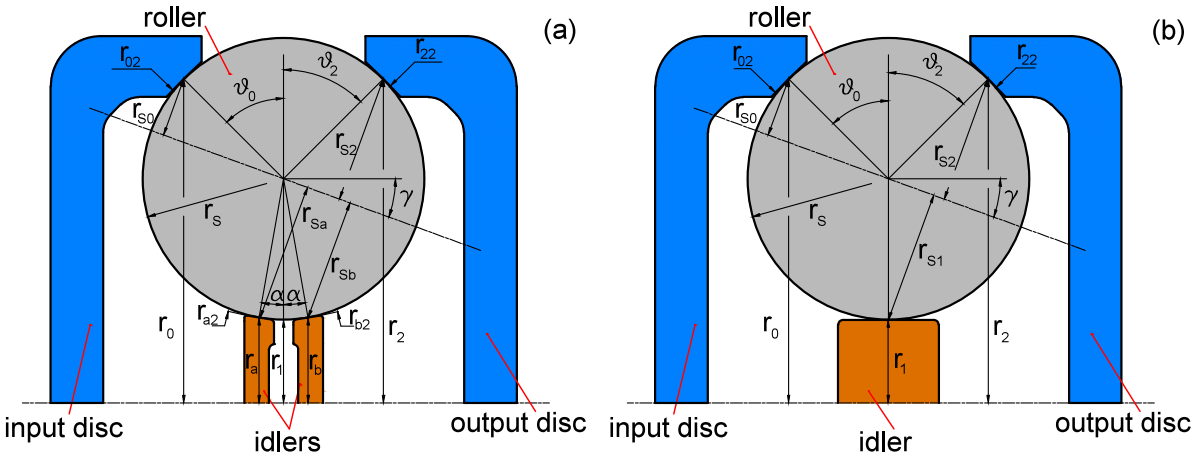

Figure 2. Schematic picture of the variator and related geometrical quantities for double-idler (a) and single-idler (b) geometries.

Hereafter, the theory is derived for the architecture comprising two inner idlers (double-idler architecture), and then it will be adapted to the single-idler architecture.

The mechanism includes the following main parts: one input and one output disc; a number N of equal spherical rollers of radius r_S, the axes of which are supported by a carrier that in the present analysis is held stationary; two equal idle discs (idlers), radially and axially supported by a common shaft which is free to slide in the axial direction. Figure 2 shows the geometrical quantities of the mechanism. Here the model is derived in the general case of unequal input and output discs. Thus, the quantities r_0 and r_2 are the radial distances of the points of contact between the roller and input and output discs respectively, from the axis of the device (in short, the input and output discs radii). Analogously, r_a and r_b are the radial distances of the points of contact between the roller and the two idlers from the main axis of the device (in short: idlers radii). In this analysis, the idlers are considered equal, i.e $r_a = r_b$. Input and output disc radii r_0 and r_2 and also the idlers radius r_i are constant quantities because the roller-discs and the roller-idlers contact points do not change location, even when the speed ratio varies. For the given sizes of the idlers, input and output discs, and the roller, three constant angles are defined, namely θ_0, θ_2 and α, as shown in Figure 2. The tilt angle of the roller axis γ is the one formed between the roller spin axis and the axial direction (horizontal in the Fig. 2): tilt angle can be varied to change the speed ratio. The distances between the spin axis of the roller and all the points of contact between the roller and the input, the output and the idlers (namely, r_{S0}, r_{S2}, r_{Sa} and r_{Sb}) are variable quantities with γ. In particular, from the Figure 2 it can be found that:

$$\begin{aligned} r_{S0} &= r_S \cos(\theta_0 + \gamma) \\ r_{Sa} &= r_S \cos(\alpha - \gamma) \\ r_{Sb} &= r_S \cos(\alpha + \gamma) \\ r_{S2} &= r_S \cos(\theta_2 - \gamma) \end{aligned} \tag{1}$$

Similarly, r_0, r_2, r_i can be also written as:

$$\begin{aligned} r_0 &= r_1 + r_S + r_S\cos\theta_0 = r_S[1 + k + \cos\theta_0] \\ r_a = r_b &= r_1 + r_S - r_S\cos\alpha = r_S[1 + k - \cos\alpha] \\ r_2 &= r_1 + r_S + r_S\cos\theta_2 = r_S[1 + k + \cos\theta_2] \end{aligned} \tag{2}$$

where r_1 is the distance between the point of the roller closest to the axis of the device (see Fig. 2) and the axis itself, and $k = r_1/r_S$ is the aspect ratio.

To complete the geometrical description of the device, we here define the quantities r_{02}, r_{a2}, r_{b2} and r_{22}, which are the second principal radii of curvature along tangential direction for the points of contact, respectively for: input disc, the idlers, and output disc, respectively.

B. Variator Kinematics

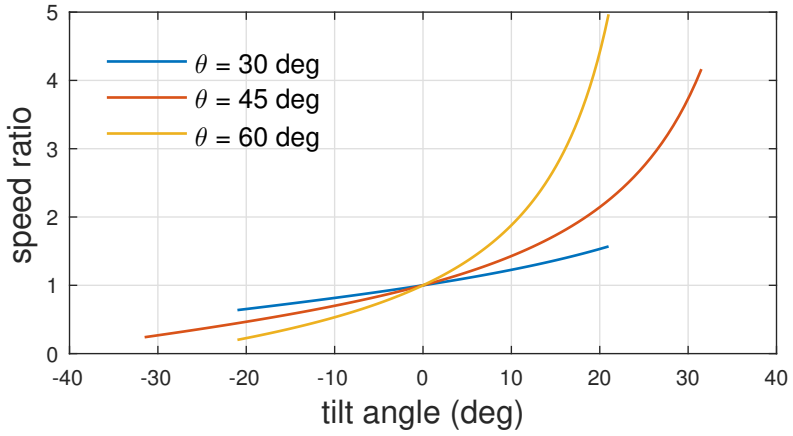

Figure 3. The ideal speed ratio τ_{ID} vs the tilt angle γ for different values of $\theta_0 = \theta_2 = \theta$.

In the case of perfect rolling contact between discs and rollers, given the angular speed of the input disc ω_0, the following kinematical relations hold:

$$\begin{aligned} \omega_0 r_0 &= \omega_S^{id} r_{S0} \\ \omega_2^{id} r_2 &= \omega_S^{id} r_{S2} \end{aligned} \tag{3}$$

where ω_0, ω_2, ω_S are the angular speeds of the input disc, the output disc and the rollers, respectively, and the superscript id means ideal, i.e. in perfect rolling contact conditions. Combining equations (1,2,3) gives the ideal speed ratio τ_{ID} as a function of the roller axis tilt angle γ:

$$\tau_{ID} = \frac{\omega_2^{id}}{\omega_0} = \frac{r_{S2} r_0}{r_{S0} r_2} = \frac{\cos(\theta_2 - \gamma)[1 + k + \cos(\theta_0)]}{\cos(\theta_0 + \gamma)[1 + k + \cos(\theta_2)]} = \tau_0 \frac{\cos(\theta_2 - \gamma)}{\cos(\theta_0 + \gamma)} \tag{4}$$

where $\tau_0 = [1 + k + \cos(\theta_0)]/[1 + k + \cos(\theta_2)]$ is a constant quantity for a given geometry. If $\theta_0 = \theta_2 = \theta$, i.e. input and output discs are equal, then the ideal speed ratio is:

$$\tau_{ID} = \frac{\cos(\theta - \gamma)}{\cos(\theta + \gamma)} \tag{5}$$

Because of geometrical constraint, the tilt angle has a range of admissible values. Specifically, referring to Fig. 2 it follows that:

$$\begin{aligned} \gamma_{min} &= \max[-\theta_0, (\theta_2 - \pi/2)] \\ \gamma_{max} &= \min[\theta_2, (\pi/2 - \theta_0)] \end{aligned} \tag{6}$$

with $\gamma_{min} \leq \gamma \leq \gamma_{max}$. The two limiting values are derived from purely geometrical constraints and it can be noted that the limit values of γ are those making $\tau_{ID} = 0$ or $\tau_{ID} = \infty$. In practice, it will also be necessary to consider the actual encumbrance of mechanical parts, like the actuation system, to define the actual limits of γ. To represent the ideal speed ratio τ_{ID} as a function of the tilt angle γ (Figure 4) given the values of $\theta_0 = \theta_2$, we have applied a safety factor of 0.8 to the limit values of γ given by eq. (6). It is there shown how the angles θ_0 and θ_2 (in case of $\theta_0 = \theta_2 = \theta$) affect the speed ratio range and the shape of the curve. The ideal speed ratio is equal to one when the tilt angle is zero, it is always positive and it is an increasing, clearly nonlinear, function of the tilt angle. It is therefore shown that the nonlinear character is emphasized as far as the speed ratio range gets larger.

1. Creep coefficients

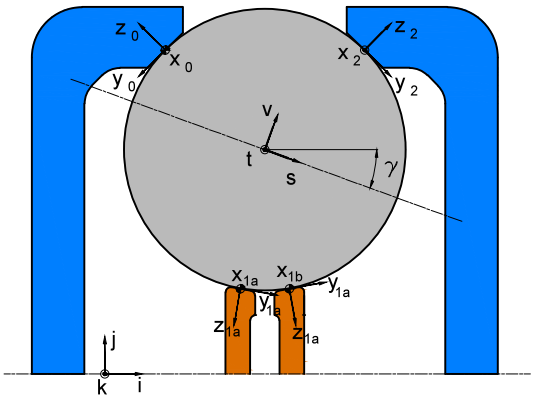

Figure 4. Schematic picture of the CVT with specification of local references.

In the real device, perfect rolling is not feasible because of some amount of creep at the contact between the rollers and the discs that always occurs when a tangential load is transmitted. Four creep coefficients are defined, one for each relevant contact pair:

$$C_{R0} = \frac{|\boldsymbol{\omega_0}|r_0 - |\boldsymbol{\omega_S}|r_{S0}}{|\boldsymbol{\omega_0}|r_0} \quad C_{Ra} = \frac{|\boldsymbol{\omega_S}|r_{Sa} - |\boldsymbol{\omega_a}|r_a}{|\boldsymbol{\omega_S}|r_{Sa}} \quad C_{Rb} = \frac{|\boldsymbol{\omega_S}|r_{Sb} - |\boldsymbol{\omega_b}|r_b}{|\boldsymbol{\omega_S}|r_{Sb}} \quad C_{R2} = \frac{|\boldsymbol{\omega_S}|r_{S2} - |\boldsymbol{\omega_1}|r_2}{|\boldsymbol{\omega_S}|r_{S2}} \tag{7}$$

Creep coefficients are a normalized measure of the tangential slip velocity at the contact, defined in principle as the difference between the tangential velocity of the moving body and the moved body, divided by the tangential velocity of the moving body. They are purely kinematic quantities that, with some exceptions as discussed below, are defined in such a way to be normally positive. The actual speed ratio can thus be written relying on eq. (7) and (4):

$$\tau_R = \frac{\omega_2}{\omega_0} = \frac{r_0 r_{S2}}{r_{S0} r_2}(1 - C_{R0})(1 - C_{R2}) = \tau_{ID}(1 - C_{R0})(1 - C_{R2}) \tag{8}$$

In some sense, creep is a measure of the speed loss of the transmission. A speed efficiency η_{speed} is thus defined:

$$\eta_{speed} = \frac{\tau_R}{\tau_{ID}} = (1 - C_{R0})(1 - C_{R2}) \tag{9}$$

2. Spin coefficients

For a given contact pair, the relative angular velocity vector of the two contacting bodies has a spin component and a tangential component. The former is obtained by projecting the relative angular velocity vector onto a direction orthogonal to the contact surfaces at the contact spot. Spin velocity causes losses in torque transmission and can generate considerable side forces on the rotating bodies [16]. By Figure 2, the relevant relative angular velocity vectors can be evaluated as follows:

$$\begin{array}{rclcl} \boldsymbol{\omega_{S0}} & = & \omega_S \mathbf{s} - \omega_0 \mathbf{j} & = & \omega_S \left(\cos\gamma \mathbf{j} - \sin\gamma \mathbf{k}\right) - \omega_0 \mathbf{j} \\ \boldsymbol{\omega_{Sa}} & = & \omega_S \mathbf{s} + \omega_a \mathbf{j} & = & \omega_S \left(\cos\gamma \mathbf{j} - \sin\gamma \mathbf{k}\right) + \omega_a \mathbf{j} \\ \boldsymbol{\omega_{Sb}} & = & \omega_S \mathbf{s} + \omega_b \mathbf{j} & = & \omega_S \left(\cos\gamma \mathbf{j} - \sin\gamma \mathbf{k}\right) + \omega_b \mathbf{j} \\ \boldsymbol{\omega_{S2}} & = & \omega_S \mathbf{s} - \omega_2 \mathbf{j} & = & \omega_S \left(\cos\gamma \mathbf{j} - \sin\gamma \mathbf{k}\right) - \omega_2 \mathbf{j} \end{array} \tag{10}$$

where the unit vectors are those defined in Figure 4. The spin velocity of two bodies in contact is the component of the relative angular velocity vector onto the normal direction evaluated at the contact point. Spin coefficients are then calculated as spin velocities normalized by a reference angular velocity modulus. Combining the definition with eqs. (7) and (10) gives the four spin coefficients are derived as functions of the tilt angle and the creep coefficients:

$$\sigma_{S0} = \frac{\boldsymbol{\omega_{S0}} \cdot \mathbf{z_0}}{|\boldsymbol{\omega_0}|} = -\tilde{r}_0 \tan(\theta_0 + \gamma)(1 - C_{R0}) + \sin\theta_0 \tag{11}$$

$$\sigma_{Sa} = \frac{\boldsymbol{\omega_{Sa}} \cdot \mathbf{z_a}}{|\boldsymbol{\omega_a}|} = -\sin\alpha - \frac{\tilde{r}_a \tan(\alpha - \gamma)}{(1 - C_{Ra})} \tag{12}$$

$$\sigma_{Sb} = \frac{\boldsymbol{\omega_{Sb}} \cdot \mathbf{z_b}}{|\boldsymbol{\omega_b}|} = \frac{\tilde{r}_b \tan(\alpha + \gamma)}{(1 - C_{Rb})} + \sin\alpha \tag{13}$$

$$\sigma_{S2} = \frac{\boldsymbol{\omega_{S2}} \cdot \mathbf{z_2}}{|\boldsymbol{\omega_2}|} = \frac{\tilde{r}_2 \tan(\theta_2 - \gamma)}{(1 - C_{R2})} - \sin\theta_2 \tag{14}$$

where the unit vectors of z-axes are defined as follows:

$$\begin{array}{rcl} \mathbf{z_0} & = & -\sin\theta_0 \mathbf{j} + \cos\theta_0 \mathbf{k} \\ \mathbf{z_{1a}} & = & -\sin\alpha \mathbf{j} - \cos\alpha \mathbf{k} \\ \mathbf{z_{1b}} & = & \sin\alpha \mathbf{j} - \cos\alpha \mathbf{k} \\ \mathbf{z_2} & = & \sin\theta_2 \mathbf{j} + \cos\theta_2 \mathbf{k} \end{array}$$

Spin coefficients are purely kinematic quantities. Spin coefficients can be positive or negative, and they are here defined in such a way to be coherently related with the spin torques defined in the next section and shown in Figure 6. Fig. 5 shows the spin coefficients as functions of the tilt angle. Calculations are performed assuming $\theta = \theta_0 = \theta_2$, $k = 1$ and no creep. Three values of θ_0 are considered which correspond to different speed ratio ranges. It can be observed that larger speed ratio ranges correspond to larger maximum values of the spin coefficients.

C. Equilibrium equations

Forces and torques equilibrium equations of each part of the variator are derived from the free-body diagrams shown in Fig. 6. A number n of equal rollers is considered. F_{D0} and F_{D2} are the clamping forces applied to input and output discs; in the free-body diagram, clamping forces are divided by n, considering the amount of them applied to each single roller. A similar argument can be discussed for the axial component of the reaction force on the inner rollers F_{Da} and F_{Db}. These are the axial component of the reaction forces of bearings. Rollers are distributed in such a way to make the outer and inner discs and the carrier radially self-equilibrated, thus radial reaction forces are zero. The normal forces F_{N0}, F_{Na}, F_{Nb} and F_{N2} are contact reaction forces between the rollers and the discs, resulting from the contact pressure distributions. Tangential forces F_{S0}, F_{Sa}, F_{Sb} and F_{S2} result from the tangential stress distribution at contact spots and enable the torque transmission. In the free-body diagrams, torques are indicated with the capital letter T. Specifically, T_0 and T_2 are the input and output (load) torques, $T_{SP0}, T_{SPa}, T_{SPb}$ and T_{SP2} are the spin torques. The bearing friction torques are T_{BLS}, T_{BLa} and T_{BLb}. Bearing friction torques are modeled according to consolidated techniques [38] [20]. There, the friction torque is calculated as the sum of two contributions: the load independent friction T_{B0}, and the load dependent friction T_{B1}. In particular, T_{B0} depends on the bearing type, the

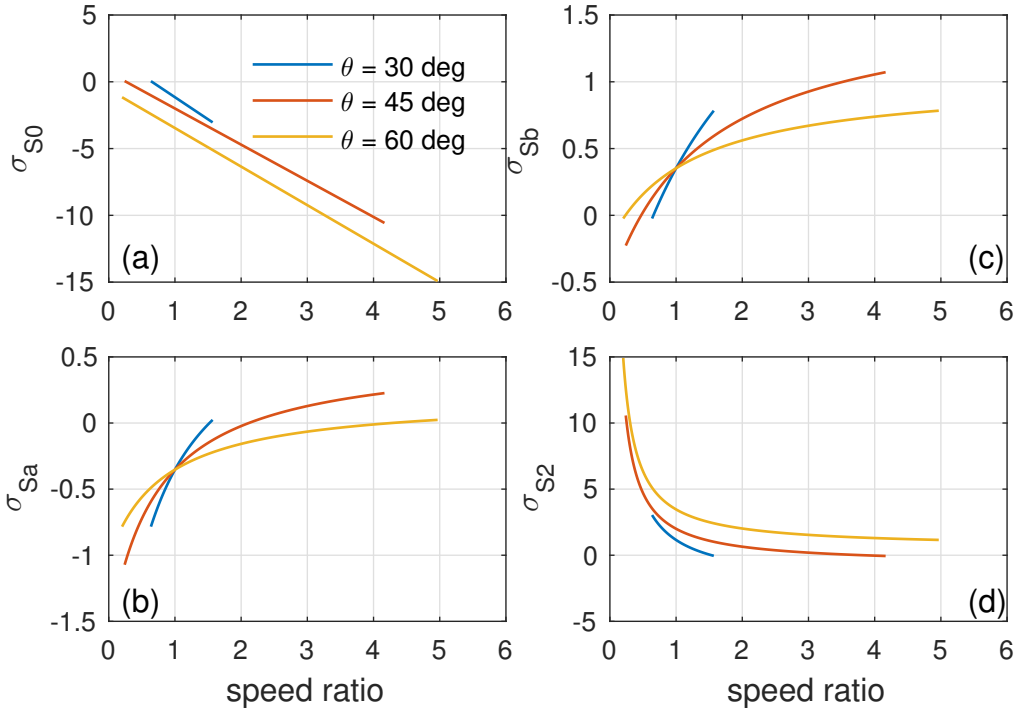

Figure 5. Spin coefficients at contacts between: (a) input disc and roller, (b) roller and first idler, (c) roller and second idler, (d) roller and output disc as functions of ideal speed ratio τ_{ID} at different values of half cone angles $\theta_0 = \theta_2 = \theta$. Aspect ratio is $k = 1$.

lubrication method and the rotational speed and is commonly determined by means of empirical formulas. In this paper, we have used the following one (see [39]):

$$T_{B0} = \begin{cases} 160 \cdot 10^{-10} f_0 d^3 & \eta_c N < 2000 \\ 10^{-10} (\eta_c N)^{0.69} f_0 d^3 & \eta_c N > 2000 \end{cases} \tag{15}$$

where $\eta_c\,[\mathrm{mm}^2/\mathrm{s}]$ is the kinematic viscosity of the lubricant, $N\,[\mathrm{RPM}]$ is the rotational speed of the bearing, $d\,[\mathrm{mm}]$ is the bearing mean diameter and $f_0 = 12$ is a coefficient that depends on the bearing type. On the other hand, the load dependent friction torque has been evaluated as follow:

$$T_{B1} = 10^{-3} f_1 P^a d_m^b \tag{16}$$

where $a = b = 1$, $f_1 = 0.003$ is a coefficient that depends on the bearing type and P is bearing load, which is calculated for each bearing by equilibrium equations.
The equilibrium of the rollers leads to the following equations:

$$\begin{aligned} &F_{S0} + F_{Sa} + F_{Sb} - F_{S2} + F_{Ra} + F_{Rb} = 0 \\ &-F_{N0}\cos\theta_0 + (F_{Na} + F_{Nb})\cos\alpha - F_{N2}\cos\theta_2 = 0 \\ &F_{N0}\sin\vartheta_0 + F_{Na}\sin\alpha - F_{Nb}\sin\alpha - F_{N2}\sin\theta_2 = 0 \end{aligned} \tag{17}$$

The torque equilibrium of the rollers gives:

$$\begin{aligned} &F_{S0} r_{S0} - F_{Sa} r_{Sa} - F_{Sb} r_{Sb} - F_{S2} r_{S2} + \\ &\quad + T_{SP0}\sin(\theta_0 + \gamma) - T_{SPa}\sin(\alpha - \gamma) + T_{SPb}\sin(\alpha + \gamma) - T_{SP2}\sin(\theta_2 - \gamma) - T_{BL} = 0 \end{aligned} \tag{18}$$

$$\begin{aligned} &F_{S0}\sin(\theta_0 + \gamma) r_B - F_{Sa}\sin(\alpha - \gamma) r_B - F_{Sb}\sin(\alpha + \gamma) r_B - F_{S2}\sin(\theta_2 - \gamma) r_B + (F_{Ra} - F_{Rb}) 0.5 r_S + \\ &\quad - T_{SP0}\cos(\theta_0 + \gamma) + T_{SPa}\cos(\alpha - \gamma) + T_{SPb}\cos(\alpha + \gamma) - T_{SP2}\cos(\theta_2 - \gamma) = 0 \end{aligned} \tag{19}$$

In eq. (19), the bearing forces on the roller F_{Ra} and F_{Rb} are supposed to be applied half-radius far from the roller center. The force and torque equilibrium of the input disc:

$$F_{D0} - nF_{N0}\sin\theta_0 = 0 \tag{20}$$
$$T_0 - nF_{S0}r_0 - nT_{SP0}\sin\theta_0 = 0 \tag{21}$$

and, equivalently of the output disc:

$$F_{D2} - nF_{N2}\sin\theta_2 = 0 \tag{22}$$
$$T_2 + nF_{S2}r_2 + nT_{SP2}\sin\theta_2 = 0 \tag{23}$$

Considering that the idlers are free to rotate, the following relations hold true:

$$F_{Da} - nF_{Na}\sin\alpha = 0 \tag{24}$$
$$T_{BLa} - nF_{Sa}r_a - nT_{SPa}\sin\alpha = 0 \tag{25}$$
$$F_{Db} - nF_{Nb}\sin\alpha = 0 \tag{26}$$
$$T_{BLb} - nF_{Sb}r_b + nT_{SPb}\sin\alpha = 0 \tag{27}$$
$$F_{Da} - F_{Db} = 0 \tag{28}$$

Force balance equations can be solved to find that all the normal contact forces and axial reaction forces are proportional to the axial applied thrust F_{N0}:

$$\begin{cases} F_{N2} = F_{N0}\frac{\sin\theta_0}{\sin\theta_2} = F_{N0} \\ F_{Na} = F_{N0}\frac{\sin(\theta_0+\theta_2)}{2\cos\alpha\sin\theta_2} = F_{N0}\frac{\cos\theta}{\cos\alpha} \\ F_{Nb} = F_{N0}\frac{\sin(\theta_0+\theta_2)}{2\cos\alpha\sin\theta_2} = F_{N0}\frac{\cos\theta}{\cos\alpha} \\ F_{D0} = nF_{N0}\sin\theta_0 = nF_{N0}\sin\theta \\ F_{Da} = nF_{N0}\tan\alpha\frac{\sin(\theta_0+\theta_2)}{2\sin\theta_2} = nF_{N0}\tan\alpha\cos\theta \\ F_{Db} = nF_{N0}\tan\alpha\frac{\sin(\theta_0+\theta_2)}{2\sin\theta_2} = nF_{N0}\tan\alpha\cos\theta \\ F_{D2} = nF_{N0}sin\theta_0 = nF_{N0}\sin\theta \end{cases} \tag{29}$$

D. Non-dimensional quantities

It is convenient to re-write the model equations in terms of non-dimensional quantities.

The tangential contact forces responsible of the torque transmissions divided by the related normal contact forces are the so called traction coefficients:

$$\begin{aligned} \mu_0 &= F_{S0}/F_{N0} \\ \mu_a &= F_{Sa}/F_{Na} \\ \mu_b &= F_{Sb}/F_{Nb} \\ \mu_2 &= F_{S2}/F_{N2} \end{aligned} \tag{30}$$

Similarly, spin coefficients are defined as follows:

$$\begin{aligned} \chi_0 &= T_{SP0}/(F_{N0}r_0) \\ \chi_a &= T_{SPa}/(F_{Na}r_a) \\ \chi_b &= T_{SPb}/(F_{Nb}r_b) \\ \chi_2 &= T_{SP2}/(F_{N2}r_2) \end{aligned} \tag{31}$$

Assuming that $\theta = \theta_0 = \theta_2$, we can rephrase the torques balance equations of outer and inner discs as it follows:

$$\begin{aligned} t_0 &= T_0/(nr_0F_{N0}) = \mu_0 + \sin(\theta)\chi_0 \\ t_{BLa} &= T_{BLa}/(nr_aF_{Na}) = \mu_a + \sin(\alpha)\chi_a \\ t_{BLb} &= T_{BLb}/(nr_bF_{Nb}) = \mu_b - \sin(\alpha)\chi_b \\ t_2 &= T_2/(nr_2F_{N2}) = -\mu_2 - \sin(\theta)\chi_2 \end{aligned} \tag{32}$$

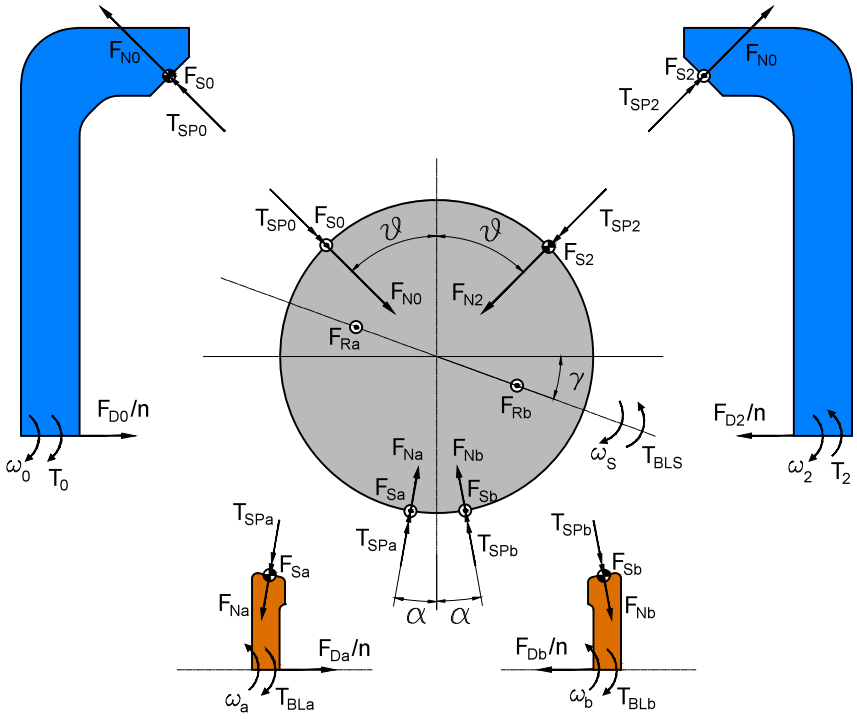

Figure 6. Free-body diagrams of the transmission parts. Single arrows are forces, double arrows are torques.

where t_0, t_{BLa}, t_{BLb}, t_2 are the non-dimensional torques on the input disc, the idlers and the output disc respectively. Similarly, using (29), the equilibrium equations of the rollers [eq. (17)] can be rephrased in non-dimensional form, which is the form used for numerical calculations:

$$\begin{aligned} t_{BLS} = {} & \tilde{r}_{S0}\mu_0 - \tilde{r}_{Sa}\tfrac{\cos\theta}{\cos\alpha}\mu_a - \tilde{r}_{Sa}\tfrac{\cos\theta}{\cos\alpha}\mu_a - \tilde{r}_{S2}\mu_2 + \\ & + \tilde{r}_0 \sin(\theta+\gamma)\chi_0 + \tilde{r}_a \tfrac{\cos\theta}{\cos\alpha}\sin(\alpha-\gamma)\chi_a - \tilde{r}_b\tfrac{\cos\theta}{\cos\alpha}\sin(\alpha+\gamma)\chi_b - \tilde{r}_2\sin(\theta-\gamma)\chi_2 \end{aligned} \tag{33}$$

$$\begin{aligned} & \sin(\theta+\gamma)\mu_0 + \tfrac{\cos\theta}{\cos\alpha}\sin(\alpha-\gamma)\mu_a - \tfrac{\cos\theta}{\cos\alpha}\sin(\alpha+\gamma)\mu_b + \sin(\theta-\gamma)\mu_2 + \tfrac{1}{2}(f_{ra}-f_{rb}) + \\ & - \tilde{r}_0\cos(\theta+\gamma)\chi_0 + \tilde{r}_a\tfrac{\cos\theta}{\cos\alpha}\cos(\alpha-\gamma)\chi_a + \tilde{r}_b\tfrac{\cos\theta}{\cos\alpha}\cos(\alpha+\gamma)\chi_b - \tilde{r}_2\cos(\theta-\gamma)\chi_2 = 0 \end{aligned} \tag{34}$$

$$\mu_0 + \tfrac{\cos\theta}{\cos\alpha}\mu_a + \tfrac{\cos\theta}{\cos\alpha}\mu_b - \mu_2 + f_{ra} + f_{rb} = 0 \tag{35}$$

where $t_{BLS} = T_{BLS}/F_{N0}r_b$.

E. Efficiency

Considering (5) and (9), we can spread the efficiency in terms of speed and torque components:

$$\eta = \frac{|P_2|}{|P_0|} = \frac{|T_2|\omega_2}{|T_0|\omega_0} = \eta_{speed}\tau_{ID}\frac{|T_2|}{|T_0|} \tag{36}$$

The quantity $\eta_{torque} = \tau_{ID}|T_2|/|T_0|$ may be rephrased using eq. (32) and (29):

$$\eta_{torque} = \tau_{ID}\frac{|T_2|}{|T_0|} = -\tau_{ID}\frac{t_2 n r_2 F_{N2}}{t_0 n r_0 F_{N0}} = \tau_{ID}\frac{\mu_2 + \chi_2\sin\theta}{\mu_0 + \chi_0\sin\theta} \tag{37}$$

Thus, the global efficiency is:

$$\eta = \left[\frac{\mu_2 + \chi_2\sin\theta}{\mu_0 + \chi_0\sin\theta}\right]\tau_{ID}(1-C_{R0})(1-C_{R2}) = \eta_{torque}\eta_{speed} \tag{38}$$

F. Calculation of traction and spin coefficients: contact model

The traction and spin coefficients can be calculated by a tribological investigation of the contacts between roller and discs. Such an analysis is carried out following the method proposed in [18]. The details of the application to the present case study are given in Appendix A.

III. SIMULATION RESULTS

A. Double-idler configuration

The mathematical model developed here can be utilized for several purposes: performance analysis, design and optimization, dynamic simulation (needs some adjustments). In this paper the focus is on the first objective, thus we carry on numerical calculations of several performance indicators of the NuVinci drive, to highlight some relevant performance differences among sightly different geometries. The geometrical parameters of the transmission analyzed in this paper are reported in Table I.

Geometric properties		Traction fluid properties	
Aspect ratio	1.7	Absolute viscosity at the atmospheric pressure	$\eta_0 = 3.25\,10^{-3}\,\mathrm{Pa\,s}$
Roller radius	$r_S = 0.03\,\mathrm{m}$	Viscosity-pressure index	$Z_1 = 0.85$
contact angle disc 0 and roller	$\theta_0 = 45°$	Pressure-viscosity coefficient	$\zeta = 1.71\,10^{-8}\,\mathrm{Pa}^{-1}$
contact angle disc 2 and roller	$\theta_2 = 45°$	Limiting shear stress at atmospheric pressure	$\tau_{L0} = 0.02\,10^{9}\,\mathrm{Pa}$
contact angle idlers-roller	$\alpha = 10°$	Limiting shear stress constant	$a = 0.085$
Number of rollers	8	Pole pressure constant of Roelands viscosity model	$c_P = 1.96\,10^{8}\,\mathrm{Pa}$
Roller bearing diameter	$d_S = 0.01\,\mathrm{m}$	Pole viscosity of Roelands viscosity model	$\eta_\infty = 6.31\,10^{-5}\,\mathrm{Pa\,s}$
Idlers bearing diameter	$d_I = 0.01\,\mathrm{m}$		

Table I. Geometrical parameters and traction fluid properties

Traction fluid properties considered in our calculations are the same as in [20], and reported in Table I.

Simulations results shown in Figure 7 are obtained under the following hypotheses: input speed is constant and equal to $\omega_0 = 2000\,\mathrm{rpm}$; the clamping force is determined in order to obtain $F_{N0} = 2.0\,\mathrm{kN}$ and it is not changed. This clamping force value leads to the maximum contact pressure equal to $p_{max} = 1.63\,\mathrm{GPa}$ at the contact between the rollers and the idlers. This value is compatible with materials adopted in roller bearings, for which the contact pressures can be up to 2-3 GPa. The simulation conditions mentioned above mimic the experimental conditions usually adopted on a test rig. In general, the output shaft of a transmission is connected to a torque-controlled brake and the input is connected to a speed-controlled motor or engine. Of course, in such contitions, when the speed ratio is increased, the output power is increased too.

The calculations are performed this way: an ideal speed ratio and an output torque request are fixed; first, the tilt angle is calculated and then all model equations are solved. Simulations start with a minimal amount of torque request, which is then gradually increased. The output torque can be increased up to a threshold value, i.e. the limiting torque, which depends on the given clamping force and the ideal speed ratio. Once such a value is reached, the simulations are stopped and then are repeated with a different value of speed ratio.

Figures 7(a-c) show the speed efficiency η_{speed}, the torque efficiency η_{torque} and the overall efficiency η of the transmission as functions of the output torque in the aforementioned conditions, i.e. with constant clamping force and input disc velocity, at three different values of constant ideal speed ratio.

Speed losses are due to the effect of creep, and so it is the speed efficiency too. If the output torque is zero, the creep is almost absent: thus, the speed efficiency is approximately equal to one, and the actual speed ratio is very close to the ideal speed ratio. A very small amount of creep is still present because of the necessity to balance small internal passive losses depending on the roller and disc speed and not on the output torque (e.g. bearing losses and spin losses). This effect is emphasized when the ideal speed ratio is large (Figure 7a). When the output torque increases, the creep must increase too: thus, the actual speed ratio is lesser than the ideal and the speed efficiency reduces as the output torque increases. The decrease is quite gradual and linear until the limiting output torque is almost reached. At this point, a very small increase of the output torque needs the creep to grow up very fast so that the speed efficiency reduces abruptly.

It can be noted that for $0.5 \leq \tau_{ID} < 1$ the limiting torque is almost independent on the τ_{ID} value, whereas when $1 < \tau_{ID} \leq 2$ the limiting torque decreases with increasing τ_{ID}. The reason is easy to explain, also with the help

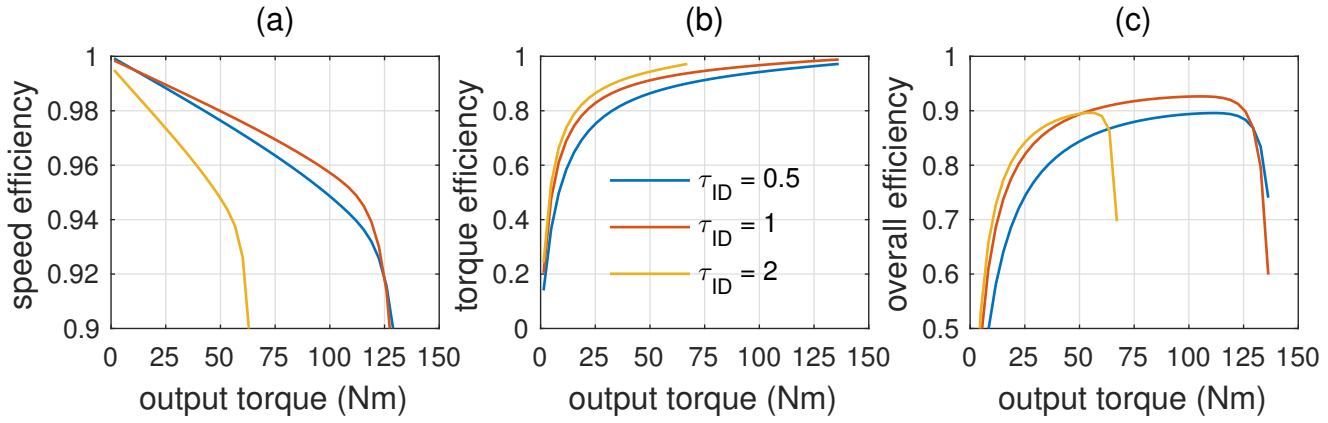

Figure 7. Speed (a), torque (b) and overall (c) efficiency as a function of output torque at different ideal speed ratio. Clamping force is constant and such that $F_{N0} = 2.0\,\mathrm{kN}$.

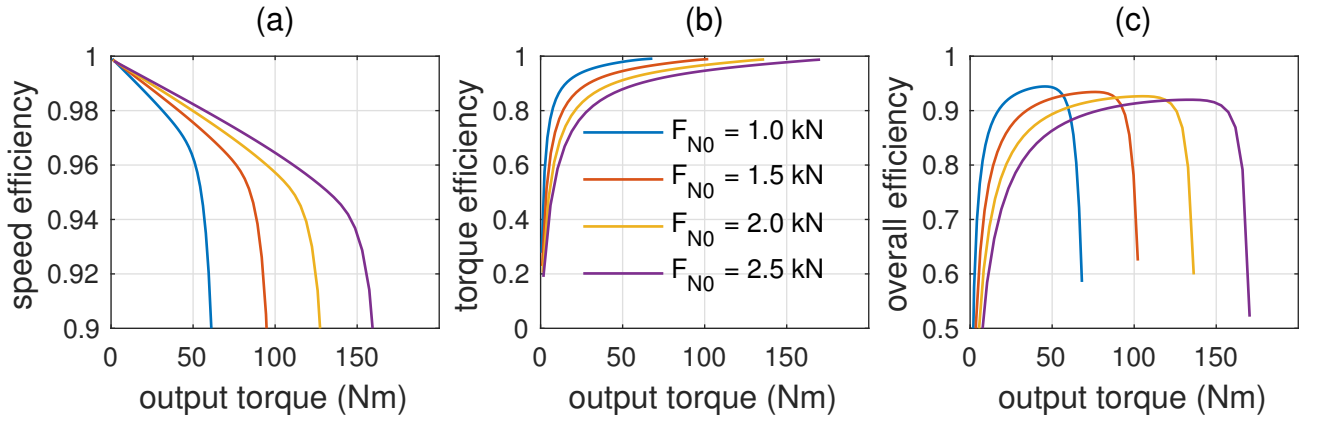

Figure 8. Speed (a), torque (b) and overall (c) efficiency as a function of output torque at different values of clamping forces. Ideal speed ratio is constant $\tau_{ID} = 1$.

of Figure 9. In the former case, the output torque must be larger than the input torque because speed ratio is less than unity (if we suppose as a first approximation that the efficiency has unit value) so the critical contact is the one between the rollers and the output torque. For the given value of clamping force, when the output torque is almost equal to 120 Nm the roller-output disc contact starts to fail, the creep coefficient at the contact between output disc and rollers increases (see Fig. 9d) and the limiting output torque is reached. In the latter case, instead, the torque on the input disc is larger than on the output disc, thus the critical contacts are those between the input discs and the rollers. For instance, when $\tau_{ID} = 2$ then $T_0 \simeq 2T_2$ i.e. when the output torque is almost equal to 60 Nm, the input torque is $\sim 120\,\mathrm{Nm}$, and the creep between input disc and rollers must increase abruptly, as confirmed in Figure 9a, thus the limiting torque is reached. Of course, when $\tau_{ID} \simeq 1$, input and output torque are very similar. Therefore, when the limiting value of the output torque is reached (i.e. $\sim 120\,\mathrm{Nm}$), the creep increases both at the input and output disc-rollers contact, as shown in Figure 9(a, d).

Figure 7c depicts the overall efficiency as a function of the output torque. The efficiency strongly depends on the output torque, with a maximum value of about 90% and a quite flat behavior in a torque range between 50% up to 90% of the limit torque. From figure 7 it emerges that at small values of output torque, the overall efficiency is very low and it very rapidly drops down to zero with decreasing torque. It can be justified by the very low and rapidly decreasing value of the torque efficiency at small values of output torque. When the output torque is relatively small, indeed, the system is over-clamped and the spin losses are too large.

However, as shown in Figure 8, this behavior depends on the clamping force. More specifically, increasing the clamping force, and thus F_{N0} , with constant $\tau_{ID} = 1$, leads to the increase of the limiting torque, the increase of the speed efficiency over the whole torque range (Figure 8a), and the reduction of the torque efficiency over the

whole torque range (Figure 8b). The combined effects emerges from Figure 8c, which plots the overall efficiency at increasing clamping force. In particular, if the clamping force is small, then the torque range is small too because of under-clamping, but the efficiency is quite large at absolute small values of output torque. On the other hand, when the clamping force is large, also the torque range is large but the efficiency is very low at absolute small values of output torque, because of over-clamping. It follows that it is possible to tune the clamping force to optimize the efficiency with respect to the desired value of the output torque. The actual efficiency curve is, in that case, the upper envelope of the efficiency curves shown in Figure 8c. Under such circumstances, the efficiency curve would be very flat with respect output torque, and values would be larger than 0.92 over the whole range.

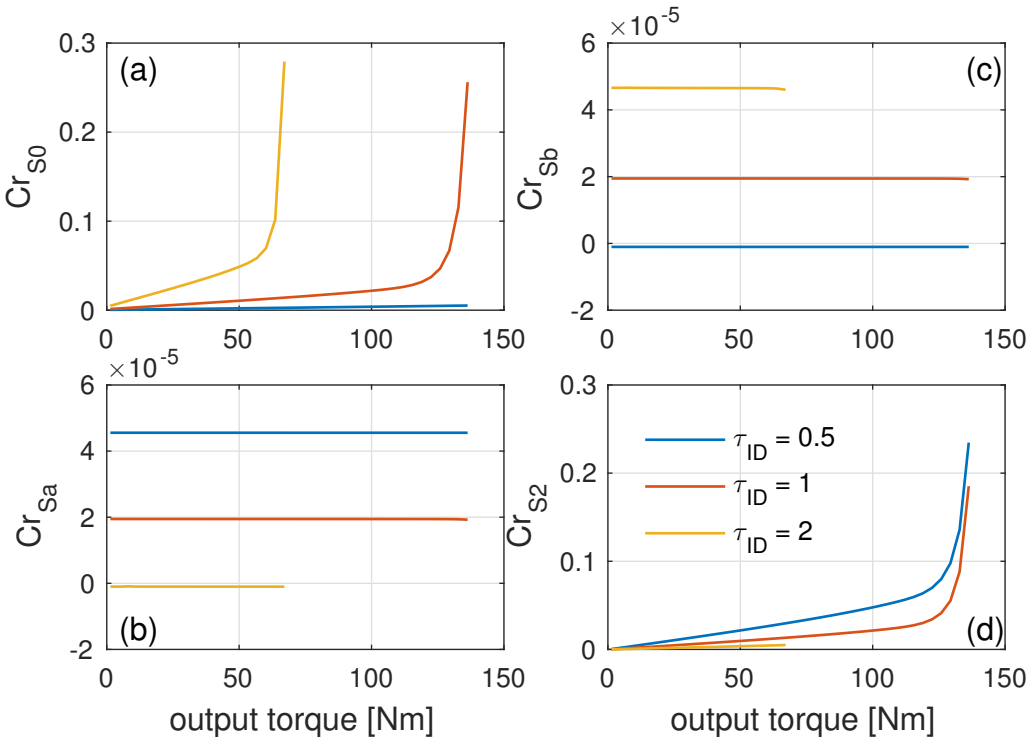

Figure 9. Creep coefficient at contacts between: (a) input disc and roller, (b) roller and first idler, (c) roller and second idler, (d) roller and output disc as functions of output torque at different vales of transmission ratio. $F_{N0} = 2.0\,\mathrm{kN}$

Interestingly, as shown in Fig. (9), some creep coefficients, namely $C_{R_{Sa}}$ and $C_{R_{Sb}}$, can drop down to negative values. To get a better insight, Figure 10a depicts the two above mentioned creep coefficients as functions of the speed ratio for an input speed $\omega_0 = 2000\,\mathrm{rpm}$ and an output torque $T_2 = 40\,\mathrm{Nm}$. In addition, we also show the spin coefficients σ_{Sa} and σ_{Sb} as functions of the ideal speed ratio and for the same operative conditions (Fig. 10b). From the figures it is also evident that the spin coefficients have a change of sign in the vicinity of the inversion points of the creep coefficients.

The inversion of a spin coefficient can be explained considering the variator geometry. In particular, the tilt angle affects the direction of the angular velocity vector of the rollers, thus the relative angular velocity between idlers and rollers depends on it. The normal component may change its sign. Accordingly, since the spin torque is always opposite wised with respect to the spin velocity, when the spin changes sign, also the spin torque must change. If we consider the idlers, as a first approximation they rotate frictionless around their axes. Therefore, in the rotational equilibrium, the spin torque axial component must be opposed by the torque given by the tangential force at idler-roller contact and thus on creep. So, under this hypotheses, when the spin changes its sign, also the creep must change. When the bearing loss is considered, things may change because the creep must equilibrate both the spin torque and the bearing torque; however, if bearing torque is small enough, then the inversion point is almost the same for spin and creep coefficients, thus a creep inversion is observed.

Of course, both spin and creep are still dissipative, even though the internal power flow changes when the creep and the spin are inverted. For instance, let us consider the contact between the roller and the first idler. In normal conditions, the roller is "faster" in the sense that its tangential velocity at the contact point is larger than the idler. In this case, the creep is positive and the power enters from the "creep side" and gets out from the "spin side". When the spin sign is inverted, the opposite power flow is achieved. However, this effect is not related to the dissipation at

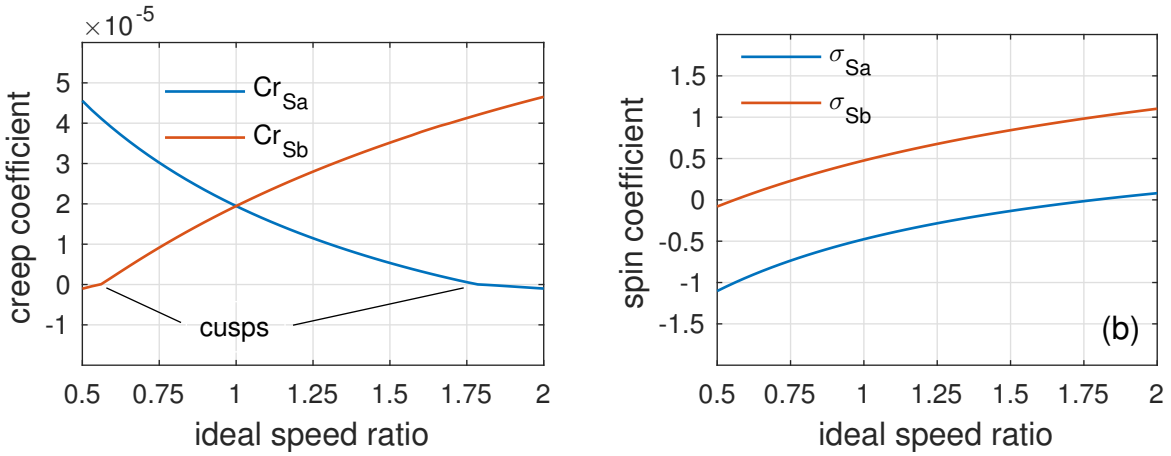

Figure 10. Creep (a) and spin (b) coefficients at contact between roller and idlers as functions of the ideal speed ratio. $F_{N0} = 2.0\,\mathrm{kN}$

contact since the power dissipated by both creep and spin depends on the relative velocities. We also calculate the overall efficiency by considering all the dissipated power terms in the device. In particular, if the power loss P_{loss} can be calculated, then the overall efficiency is given by:

$$\eta = 1 - \frac{P_{loss}}{P_0} = 1 - \frac{P_{loss}}{T_0 \omega_0} \tag{39}$$

where P_{loss} can be calculated as the sum of the creep loss P_{CR}, the spin loss P_{SP} and bearing loss P_{BL}:

$$\begin{aligned} P_{CR} &= n\left(|\omega_0 r_0 C_{R0} F_{S0}| + |\omega_S r_{Sa} C_{Ra} F_{Sa}| + |\omega_S r_{Sb} C_{Rb} F_{Sb}| + |\omega_S r_{S2} C_{R2} F_{S2}|\right) \\ P_{SP} &= n\left(|T_{SP0}\sigma_{S0}\omega_0| + |T_{SPa}\sigma_{Sa}\omega_a| + |T_{SPb}\sigma_{Sb}\omega_b| + |T_{SP2}\sigma_{S2}\omega_2|\right) \\ P_{BL} &= n\left(|T_{SBL}\omega_S| + |T_{BLa}\omega_a| + |T_{BLb}\omega_b|\right) \\ P_{loss} &= P_{CR} + P_{SP} + P_{BL} \end{aligned} \tag{40}$$

Figure 11 shows the overall efficiency of the transmission calculated by eq. 38 and by eq. 39, as a function of the ideal speed ratio and for given values of the output torque $T_2 = 40\,\mathrm{Nm}$ and input speed $\omega_0 = 2000\,\mathrm{rpm}$. The maximum efficiency almost equals 0.89, and this value is achieved at $\tau_{ID} \simeq 1.76$. The efficiency starts from 0.82 and $\tau_{ID} = 0.5$ and has a quite slow growth, up to the maximum value. There are two points in which the curve slope undergoes step changes: they are very close to the spin coefficients inversion points. It is worth noting that the two methodologies used to calculate the efficiency lead to equal results.

B. Single-idler configuration

The analysis on the power flow between the roller and the inner disc leads to the conclusion that, at least when the inner disc bearing losses are negligible, there is a certain amount of creep which is due to the axial component of spin. Therefore, a geometry of the contact between the roller and the inner disc which vanishes the axial component of the spin could be much better in terms of power dissipation and efficiency, since it will necessarily reduce the creep too. Thus, we analyzed the geometry shown in Figure 2b, where the inner discs are replaced by one single annulus giving radial support to the rollers. In this conditions, there is already a spin torque and, consequently, a spin dissipation at the contact between the roller and the inner annulus; however, the creep is expected to be limited since the spin has no axial component on the inner annulus. Further, also bearing losses on inner annulus are much smaller since there is no radial or axial load to be supported by bearings, and the loss is only due to bearing rotational speed.

Figure 12 shows the creep coefficient as a function of the ideal speed ratio. The largest values of creep correspond to the extremes of the ratio range, which also correspond to the maximum values of the spin ratio. However, as expected, the maximum creep is two orders of magnitude smaller than obtained in the double-roller geometry (Figure 10) and, accordingly, the overall creep loss is also expected to be smaller. More importantly, the spin has no axial component in the central element, resulting in a larger torque efficiency. At $\tau_{ID} = 1$ it is also obtained that $\sigma_{S1} = 0$,

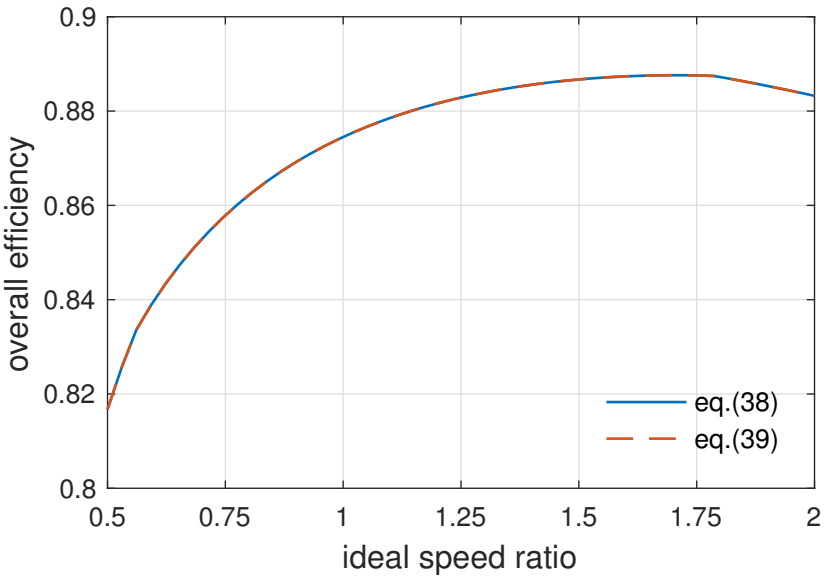

Figure 11. Overall efficiency of the transmission vs ideal speed ratio. The efficiency values are calculated by the eq. (38) and by the eq. (39) for comparison. $F_{N0} = 2.0\,\mathrm{kN}$

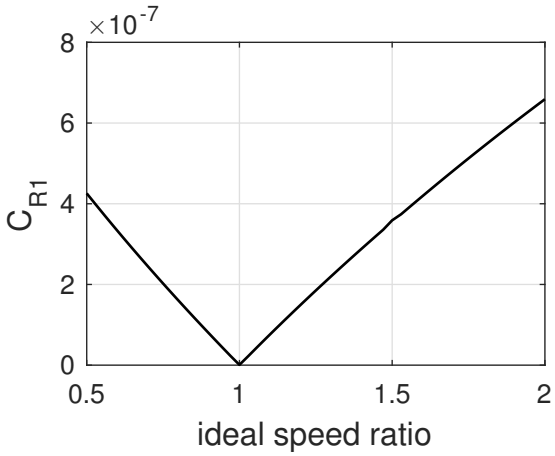

Figure 12. Creep coefficient on the single-idler as a function of speed ratio. $F_{N0} = 2.0\,\mathrm{kN}$

so at $\tau_{ID} = 1$ the variator is expected to have a large efficiency. Figure (13) shows the efficiency of the single-roller configuration in comparison with the double-roller, with $\omega_0 = 2000\,\mathrm{rpm}$, $T_2 = 20$, 40, 60 Nm and a thrust force such that $F_{N0} = 2.0\,\mathrm{kN}$. Observing the figure we can note that efficiency is quite larger over the whole range of τ_{ID} if the two idlers are replaced by a single one, whatever the value of the output torque. In particular, when $\tau_{ID} = 1$ the efficiency is maximum and the difference between the single and the double-roller is maximum too; in such a point the spin σ_{S1} is equal to zero and, consequently, also the spin power dissipation in the contact between the roller and the idler must vanish in the single-idler architecture.

The drawback of this configuration is that the maximum pressure of contact at the contact between the rollers and the idler is larger for an equal value of clamping force. Indeed, in the case analyzed herein, with a clamping force equal to 2.0 kN the maximum contact pressure is equal to 2.61 GPa (we remember that 1.63 GPa was the maximum value on the double roller architecture at equal clamping force). The reasons are: In this case only one contact must sustain all the radial load; The contact area is smaller because of a smaller equivalent radius of contact. This makes the maximum admissible clamping force, and thus output torque, smaller for the single-idler than for the double idler.

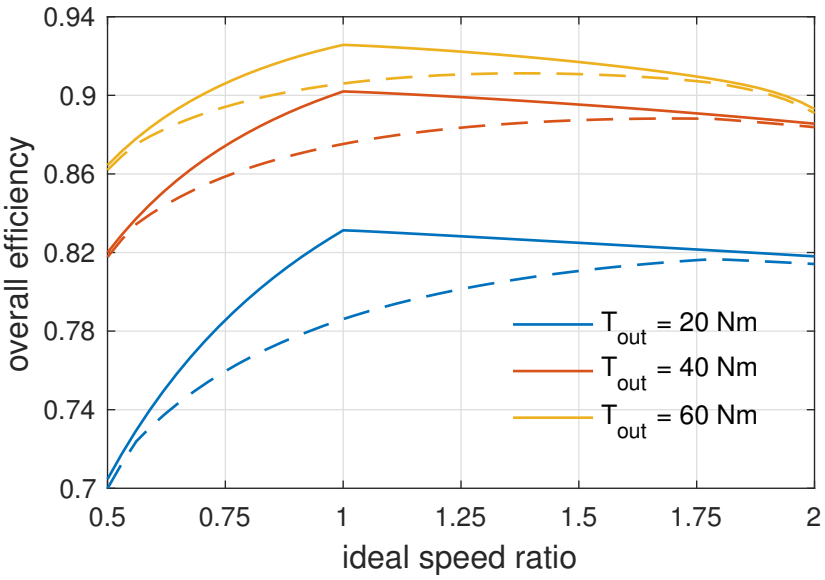

Figure 13. Drive efficiency: comparison between the double-idler architecture and the single-idler architecture. Efficiency is shown as a function of the ideal speed ratio with constant output torques (values in the legend). $F_{N0} = 2.0\,\mathrm{kN}$.

IV. CONCLUSIONS

The following achievements are worthy of being mentioned:

- A mathematical model of a NuVinci drive has been developed, which is based upon a kinematic analysis, equilibrium equations, and a tribological model of contacts. The model enables the calculation of the traction capabilities of a device of a given geometry, and the estimation of the speed and torque efficiency of the traction drive, allowing simulating the overall drive efficiency.

- Two different architectures are considered. The first one comes from a geometrical analysis of a real device purchased and disassembled on purpose; such architecture is named double-idler since the ball rollers are radially restrained by a couple of idlers set in the inner part of the device. The second one comes from the original patent (see Ref. [27]) and named single-idler because the rollers are radially restrained by one single cylindrical idler in the inner part. There is no difference in principle in terms of model construction.

- It is found that, for one given value of the thrust force, the efficiency of the single-idler architecture is larger than the double-idler over the entire range of speed ratio, with a peak efficiency of 0.9 when speed ratio is equal to one. Here, the peak difference with respect to the double idler is found and it is of about 3% of efficiency. At this point in the single-idler architecture, the roller-idler contact is spin-less.

- The reason of such an evident difference is investigated, and set in relation to two factors. First, in the case of double-idler architecture, there is no speed ratio leading to an overall zero-spin condition at roller-idler contact. Second, the axial amount of spin at roller-idlers contact leads also a small amount of creep. A kind of internal power circulation arises which increases the power loss further.

Further investigations are planned to study the behavior of the NuVinci as a CVP, to compare the foreseen behavior with experimental results and to add dynamic effects.

APPENDIX A

The development of a contact model that takes into account the viscoelastic behavior of traction fluid is a mandatory step to define the traction coefficients, the spin coefficients and thus the creep and the efficiency. The model adopted for this purpose was developed in [18]. According to this model, considering the high contact pressure it is reasonable to suppose that the pressure distribution is given by Hertzian theory for dry contact. The film thickness of the traction

oil is estimated using the Hamrock-Dowson formula for hard-EHL contact, and it is supposed to be almost constant in the contact area [40].

The first step to calculate the contact area and pressure distribution according to the theory of Hertz is to evaluate the equivalent radius of curvature of the surfaces in the point of contact. The equivalent radius of curvature in dimensionless form is $\tilde{\rho}_j^{eq} = (r_S/\rho_{j,x}^{eq} + r_S/\rho_{j,y}^{eq})^{-1}$, where $\rho_{j,x}^{eq}$ and $\rho_{j,y}^{eq}$ are the equivalent radii of curvature in the rolling and tilting direction respectively and j indicates the j-th contact. The equivalent contact radii in the rolling and tilting directions are thus calculated for every contact:

$$\tilde{\rho}_{0,x}^{eq} = \frac{1}{r_S}\left(\frac{1}{r_{0,x}} + \frac{1}{r_{S0,x}}\right)^{-1} = \frac{\tilde{r}_0}{1+k}; \qquad \tilde{\rho}_{0,y}^{eq} = \frac{1}{r_S}\left(\frac{1}{r_{0,y}} + \frac{1}{r_{S0,y}}\right)^{-1} = \frac{\tilde{r}_{02}-1}{\tilde{r}_{02}} \tag{41}$$

$$\tilde{\rho}_{a,x}^{eq} = \frac{1}{r_S}\left(\frac{1}{r_{a,x}} + \frac{1}{r_{Sa,x}}\right)^{-1} = \frac{\tilde{r}_a}{1+k}; \qquad \tilde{\rho}_{a,y}^{eq} = \frac{1}{r_S}\left(\frac{1}{r_{a,y}} + \frac{1}{r_{Sa,y}}\right)^{-1} = \frac{\tilde{r}_{a2}-1}{\tilde{r}_{a2}} \tag{42}$$

$$\tilde{\rho}_{b,x}^{eq} = \frac{1}{r_S}\left(\frac{1}{r_{b,x}} + \frac{1}{r_{Sb,x}}\right)^{-1} = \frac{\tilde{r}_b}{1+k}; \qquad \tilde{\rho}_{b,y}^{eq} = \frac{1}{r_S}\left(\frac{1}{r_{b,y}} + \frac{1}{r_{Sb,y}}\right)^{-1} = \frac{\tilde{r}_{b2}-1}{\tilde{r}_{b2}} \tag{43}$$

$$\tilde{\rho}_{2,x}^{eq} = \frac{1}{r_S}\left(\frac{1}{r_{2,x}} + \frac{1}{r_{S2,x}}\right)^{-1} = \frac{\tilde{r}_2}{1+k}; \qquad \tilde{\rho}_{2,y}^{eq} = \frac{1}{r_S}\left(\frac{1}{r_{2,y}} + \frac{1}{r_{S2,y}}\right)^{-1} = \frac{\tilde{r}_{22}-1}{\tilde{r}_{22}} \tag{44}$$

Where $\tilde{r}_k = r_k/r_S$ with $k = 0, a, b, 2, 02, a2, b2, 22$. The Hertzian contact area is elliptical and to evaluate the contact pressure distribution it is necessary to calculate the semi axes of contact ellipse (a_x and a_y). The Hamrock and Brewe method [40] is thus followed. Eccentricity parameter ϵ and elliptic integrals I_1 and I_2 are defined as follow:

$$\epsilon = \frac{\tilde{a}_y}{\tilde{a}_x} = \xi^{2/\pi} \tag{45}$$

$$I_1 = \begin{cases} \frac{\pi}{2} - \left(\frac{\pi}{2} - 1\right)\ln(\xi) & \epsilon < 1 \\ \frac{\pi}{2} + \left(\frac{\pi}{2} - 1\right)\ln(\xi) & \epsilon > 1 \end{cases} \tag{46}$$

$$I_2 = \begin{cases} 1 + \left(\frac{\pi}{2} - 1\right)\xi & \epsilon < 1 \\ 1 + \left(\frac{\pi}{2} - 1\right)\frac{1}{\xi} & \epsilon > 1 \end{cases} \tag{47}$$

where the dimensionless coefficient ξ is given by $\xi = \rho_y^{eq}/\rho_x^{eq}$. Dimensionless axes $\tilde{a}_x$ and $\tilde{a}_y$ in (45) are evaluated as a_x/Λ and a_y/Λ where the contact length parameter Λ is:

$$\Lambda = \left(\frac{6F_n r_S}{\pi E'}\right)^{\frac{1}{3}} \tag{48}$$

In the eq. (48) $E' = E/(1-\nu^2)$, E and ν are the modulus of elasticity of the contacting bodies and the Poisson ratio, respectively. The contact length parameter is evaluated for each point of contact, to simplify the discussion and considering that the definition of the following quantities are the same for every point of contact, here in after we avoid the use of the subscript (where unnecessary).

Equations (41) to (48) allow us to evaluate dimensionless semi-axes of contact eclipse for the three points of contact:

$$\tilde{a}_y = \left(\epsilon^2 I_2 \tilde{\rho}_y^{eq}\right)^{\frac{1}{3}}; \qquad \tilde{a}_x = \left(I_2 \frac{\tilde{\rho}_x^{eq}}{\epsilon}\right)^{\frac{1}{3}} \tag{49}$$

Using the results of Hertzian theory [40], introducing half-amplitude of the subsurface orthogonal shear stress $\tilde{\tau}_0 = \tau_0 \Lambda^2/F_n$ and the dimensionless co-ordinates $X = x/a_x$ and $Y = y/a_y$, we can define the dimensionless pressure distribution as follow:

$$\tilde{p}_Y = \tilde{p}_{max}\sqrt{1 - X^2 - Y^2} = \frac{3}{2\pi \tilde{a}_X \tilde{a}_Y}\sqrt{1 - X^2 - Y^2} \tag{50}$$

The pressure-dependent fluid viscosity for EHL contact is calculated through the following formula:

$$\log(\tilde{\eta}) = \log(\eta/\eta_0) = \left[\left(1 + \frac{\pi\tilde{p}}{6\Re\tilde{c}_p}\right)^{z_1} - 1\right]\log(\eta_0/\eta_\infty) \tag{51}$$

Where $\tilde{c}_p = c_p E'$, $c_p = 1.96 \cdot (10)^8$, η is the absolutely viscosity at the pressure p, η_0 is the absolute viscosity at the atmospheric pressure for the given temperature, $\eta_\infty = 6.31 \cdot 10^{-5}\,\mathrm{Pa\,s}$, the dimensionless constant z_1 is the viscosity-pressure index and $\Re$ is the dimensionless load parameter:

$$\Re = \frac{r_S}{\Lambda} = \left(\frac{\pi E' r_S^2}{6F_n}\right)^{1/3} \tag{52}$$

Using the procedure presented in [18, 20], the shear stress acting on the roller at the contacts point in rolling and tangential directions are thus defined:

$$\begin{aligned}
\tilde{\tau}_{S0,x} &= \frac{6}{\pi}\Re_0\tilde{\tau}_{L0}\frac{v_{S0,x}}{|\boldsymbol{V_{S0}}|}\left(1 - e^{-\frac{\eta_{S0}|\boldsymbol{V_{S0}}|}{h_0\tau_{L0}}}\right); \qquad \tilde{\tau}_{S0,y} = \frac{6}{\pi}\Re_0\tilde{\tau}_{L0}\frac{v_{S0,y}}{|\boldsymbol{V_{S0}}|}\left(1 - e^{-\frac{\eta_{S0}|\boldsymbol{V_{S0}}|}{h_0\tau_{L0}}}\right)\\
\tilde{\tau}_{Sa,x} &= \frac{6}{\pi}\Re_a\tilde{\tau}_{La}\frac{v_{Sa,x}}{|\boldsymbol{V_{Sa}}|}\left(1 - e^{-\frac{\eta_{Sa}|\boldsymbol{V_{Sa}}|}{h_a\tau_{La}}}\right); \qquad \tilde{\tau}_{Sa,y} = \frac{6}{\pi}\Re_a\tilde{\tau}_{La}\frac{v_{Sa,y}}{|\boldsymbol{V_{Sa}}|}\left(1 - e^{-\frac{\eta_{Sa}|\boldsymbol{V_{Sa}}|}{h_a\tau_{La}}}\right)\\
\tilde{\tau}_{Sb,x} &= \frac{6}{\pi}\Re_b\tilde{\tau}_{Lb}\frac{v_{Sb,x}}{|\boldsymbol{V_{Sb}}|}\left(1 - e^{-\frac{\eta_{Sb}|\boldsymbol{V_{Sb}}|}{h_b\tau_{Lb}}}\right); \qquad \tilde{\tau}_{Sb,y} = \frac{6}{\pi}\Re_b\tilde{\tau}_{Lb}\frac{v_{Sb,y}}{|\boldsymbol{V_{Sb}}|}\left(1 - e^{-\frac{\eta_{Sb}|\boldsymbol{V_{Sb}}|}{h_b\tau_{Lb}}}\right)\\
\tilde{\tau}_{S2,x} &= \frac{6}{\pi}\Re_2\tilde{\tau}_{L2}\frac{v_{S2,x}}{|\boldsymbol{V_{S2}}|}\left(1 - e^{-\frac{\eta_{S2}|\boldsymbol{V_{S2}}|}{h_2\tau_{L2}}}\right); \qquad \tilde{\tau}_{S2,y} = \frac{6}{\pi}\Re_2\tilde{\tau}_{L2}\frac{v_{S2,y}}{|\boldsymbol{V_{S2}}|}\left(1 - e^{-\frac{\eta_{S2}|\boldsymbol{V_{S2}}|}{h_2\tau_{L2}}}\right)
\end{aligned} \tag{53}$$

where h_j is the film thickness of the oil in the point of contact (at contact j-th), while $\tilde{\tau}_{Lj} = \tau_{Lj}/E'$ and τ_{Lj} is the limiting shear stress at contact j-th calculated as:

$$\tau_{Lj} = \tau_L^0 + ap \tag{54}$$

where τ_L^0 is the limiting shear stress at atmospheric pressure. Dimensionless relative velocities of eq. (53) can be evaluated:

$$\begin{aligned}
\frac{v_{S0,x}}{|\boldsymbol{\omega_0}|r_0} &= C_{R0} - \frac{\sigma_{S0}\tilde{a}_{0,y}Y}{\tilde{r}_0\Re_0}; \qquad \frac{v_{S0,y}}{|\boldsymbol{\omega_0}|r_0} = \frac{\sigma_{S0}\tilde{a}_{0,x}X}{\tilde{r}_0\Re_0}\\
\frac{v_{Sa,x}}{|\boldsymbol{\omega_a}|r_a} &= \frac{C_{Ra}}{1 - C_{Ra}} - \frac{\sigma_{Sa}\tilde{a}_{a,y}Y}{\tilde{r}_a\Re_a}; \quad \frac{v_{Sa,y}}{|\boldsymbol{\omega_a}|r_a} = \frac{\sigma_{Sa}\tilde{a}_{a,x}X}{\tilde{r}_a\Re_a}\\
\frac{v_{Sb,x}}{|\boldsymbol{\omega_b}|r_b} &= \frac{C_{Rb}}{1 - C_{Rb}} - \frac{\sigma_{Sb}\tilde{a}_{b,y}Y}{\tilde{r}_b\Re_b}; \quad \frac{v_{SbY}}{|\boldsymbol{\omega_b}|r_b} = \frac{\sigma_{Sb}\tilde{a}_{b,x}X}{\tilde{r}_b\Re_b}\\
\frac{v_{S2,x}}{|\boldsymbol{\omega_2}|r_2} &= \frac{C_{R2}}{1 - C_{R2}} - \frac{\sigma_{S2}\tilde{a}_{2,y}Y}{\tilde{r}_2\Re_2}; \quad \frac{v_{S2,y}}{|\boldsymbol{\omega_2}|r_2} = \frac{\sigma_{S2}\tilde{a}_{2,x}X}{\tilde{r}_2\Re_2}
\end{aligned} \tag{55}$$

Eqs. (53) need the value of the film thickness to be solved. Using the Hamrock model for elliptical conjunction in EHL contact, we can calculate the dimensionless central film thickness $H = h/\rho_x^{eq}$ of lubricant in the contact region as follows:

$$\begin{aligned}
H_0 &= 2.69\left(\frac{\pi}{6}\right)^{-0.067}\left[(1 - 0.5C_{r0})(1 + k)\tilde{\omega}_0\right]^{0.67}\tilde{\zeta}^{\,0.53}\,\tilde{\rho}_{0,x}^{eq\;0.134}\,\Re_0^{\,0.201}\,\left(1 - 0.61e^{-0.73\epsilon_0}\right)\\
H_a &= 2.69\left(\frac{\pi}{6}\right)^{-0.067}\left[\left(\frac{1 - 0.5C_{ra}}{1 - C_{ra}}\right)(1 + k)\tilde{\omega}_a\right]^{0.67}\tilde{\zeta}^{\,0.53}\,\tilde{\rho}_{a,x}^{eq\;0.134}\,\Re_a^{\,0.201}\,\left(1 - 0.61e^{-0.73\epsilon_a}\right)\\
H_b &= 2.69\left(\frac{\pi}{6}\right)^{-0.067}\left[\left(\frac{1 - 0.5C_{rb}}{1 - C_{rb}}\right)(1 + k)\tilde{\omega}_b\right]^{0.67}\tilde{\zeta}^{\,0.53}\,\tilde{\rho}_{b,x}^{eq\;0.134}\,\Re_b^{\,0.201}\,\left(1 - 0.61e^{-0.73\epsilon_a}\right)\\
H_2 &= 2.69\left(\frac{\pi}{6}\right)^{-0.067}\left[\left(\frac{1 - 0.5C_{r2}}{1 - C_{r2}}\right)(1 + k)\tilde{\omega}_2\right]^{0.67}\tilde{\zeta}^{\,0.53}\,\tilde{\rho}_{2x}^{eq\;0.134}\,\Re_2^{\,0.201}\,\left(1 - 0.61e^{-0.73\epsilon_2}\right)
\end{aligned} \tag{56}$$

Given all these quantities, traction and spin coefficients can be calculated. The elemental tangential force is express by means of shear stress in rolling direction as:

$$dF_{Si} = \tau_{Si,x} dA = \tau_{Si,x} dx dy; \qquad i = \{0, a, b, 2\} \tag{57}$$

While, according the relations from (63) to (66), the spin torque is evaluated as:

$$dT_{SPi} = (\tau_{Si,y} x - \tau_{Si,x} y)\, dx dy; \qquad i = \{0, a, b, 2\} \tag{58}$$

Combining (59) to (66) with (57) and (58), traction and spin coefficients are calculated:

$$\mu_0 = \tilde{a}_{0,x} \tilde{a}_{0,y} \int_0^1 dR \int_0^{2\pi} \tilde{\tau}_{S0,x} R d\psi \tag{59}$$

$$\mu_a = \tilde{a}_{a,x} \tilde{a}_{a,y} \int_0^1 dR \int_0^{2\pi} \tilde{\tau}_{Sa,x} R d\psi \tag{60}$$

$$\mu_b = \tilde{a}_{b,x} \tilde{a}_{b,y} \int_0^1 dR \int_0^{2\pi} \tilde{\tau}_{Sb,x} R d\psi \tag{61}$$

$$\mu_2 = \tilde{a}_{2,x} \tilde{a}_{2,y} \int_0^1 dR \int_0^{2\pi} \tilde{\tau}_{S2,x} R d\psi \tag{62}$$

$$\chi_0 = \frac{\tilde{a}_{0,x} \tilde{a}_{0,y}}{\mathfrak{R}_0 \tilde{r}_0} \int_0^1 dR \int_0^{2\pi} \phi_0(R, \psi) R^2 d\psi \tag{63}$$

$$\chi_a = \frac{\tilde{a}_{a,x} \tilde{a}_{a,y}}{\mathfrak{R}_a \tilde{r}_a} \int_0^1 dR \int_0^{2\pi} \phi_a(R, \psi) R^2 d\psi \tag{64}$$

$$\chi_b = \frac{\tilde{a}_{b,x} \tilde{a}_{b,y}}{\mathfrak{R}_b \tilde{r}_b} \int_0^1 dR \int_0^{2\pi} \phi_b(R, \psi) R^2 d\psi \tag{65}$$

$$\chi_2 = \frac{\tilde{a}_{2,x} \tilde{a}_{2,y}}{\mathfrak{R}_2 \tilde{r}_2} \int_0^1 dR \int_0^{2\pi} \phi_2(R, \psi) R^2 d\psi \tag{66}$$

where $\phi_i(R, \psi) = (\tilde{\tau}_{Si,y} \cos(\psi) - \tilde{\tau}_{Si,x} \sin(\psi))$, $\tilde{\tau}_{Six}$ and $\tilde{\tau}_{Siy}$ are respectively, the shear stress in the rolling direction and along the normal direction for each point of contact. $\mathfrak{R}$ is the load factor that depends on the geometry and the normal force. $\tilde{a}_X$ and $\tilde{a}_Y$ are the axes length of the elliptic contact in dimensionless form.

ACKNOWLEDGMENTS

This work was supported by the Italian Ministry of Education, University and Research under the Program "Department of Excellence" Legge 232/2016 (Grant No. CUP - D94I18000260001)

[1] M. A. Kluger, D. M. Long, An overview of current automatic, manual and continuously variable transmission efficiencies and their projected future improvements, in: International Congress and Exposition, SAE International, 1999.
[2] N. Sclater, N. P. Chironis, Mechanisms and mechanical devices sourcebook, Vol. 4, McGraw-Hill New York, 2007.
[3] N. Srivastava, I. Haque, A review on belt and chain continuously variable transmissions (cvt): Dynamics and control, Mechanism and machine theory 44 (1) (2009) 19–41.

[4] S. Akehurst, D. Parker, S. Schaaf, Cvt rolling traction drives - a review of research into their design, functionality, and modeling, Journal of Mechanical Design 128 (5) (2006) 1165–1176.

[5] L. O. Hewko, Automotive traction drive cvts-an overview, Tech. rep., SAE Technical Paper (1986).

[6] G. Carbone, L. Mangialardi, G. Mantriota, The influence of pulley deformations on the shifting mechanism of metal belt cvt, Journal of mechanical design 127 (1) (2005) 103–113.

[7] G. Carbone, L. Mangialardi, B. Bonsen, C. Tursi, P. Veenhuizen, Cvt dynamics: Theory and experiments, Mechanism and Machine Theory 42 (4) (2007) 409 – 428.

[8] G. Carbone, L. De Novellis, G. Commissaris, M. Steinbuch, An enhanced cmm model for the accurate prediction of steady-state performance of cvt chain drives, Journal of Mechanical Design 132 (2) (2010) 021005.

[9] G. Carbone, L. Mangialardi, G. Mantriota, Theoretical model of metal v-belt drives during rapid ratio changing, Journal of Mechanical Design 123 (1) (2001) 111–117.

[10] A. Yildiz, A. Piccininni, F. Bottiglione, G. Carbone, Modeling chain continuously variable transmission for direct implementation in transmission control, Mechanism and Machine Theory 105 (2016) 428–440.

[11] A. Yildiz, F. Bottiglione, A. Piccininni, O. Kopmaz, G. Carbone, Experimental validation of the carbone–mangialardi–mantriota model of continuously variable transmissions, Proceedings of the Institution of Mechanical Engineers, Part D: Journal of Automobile Engineering 232 (6) (2018) 828–837.

[12] H. Tanaka, J. Yokohama, Aspect of variator control of half-toroidal cvt, VDI BERICHTE 1709 (2002) 23–34.

[13] H. Tanaka, Speed ratio control of a parallel layout double cavity half-toroidal cvt for four-wheel drive, JSAE review 23 (2) (2002) 213–217.

[14] M. Patterson, Paper x (iv) traction drive contact optimisation, in: Tribology Series, Vol. 18, Elsevier, 1991, pp. 295–300.

[15] M. Patterson, The full-toroidal variator in theory and in practice, in: Proceedings of the International Conference on Continuously Variable Power Transmissions, Yokohama, 1996, pp. 95–100.

[16] S. H. Loewenthal, Spin analysis of concentrated traction contacts., Journal of mechanisms, transmissions, and automation in design 108 (1) (1986) 77–85.

[17] F. Verbelen, S. Derammelaere, P. Sergeant, K. Stockman, Half toroidal continuously variable transmission: Trade-off between dynamics of ratio variation and efficiency, Mechanism and Machine Theory 107 (2017) 183–196.

[18] G. Carbone, L. Mangialardi, G. Mantriota, A comparison of the performances of full and half toroidal traction drives, Mechanism and Machine Theory (2004) 921–942.

[19] F. the, S. Derammelaere, P. Sergeant, K. Stockman, A comparison of the full and half toroidal continuously variable transmissions in terms of dynamics of ratio variation and efficiency, Mechanism and Machine Theory 121 (2018) 299 – 316.

[20] L. De Novellis, G. Carbone, L. Mangialardi, Traction and efficiency performance of the double roller full-toroidal variator: A comparison with half- and full-toroidal drives, Journal of Mechanical Design, Transactions Of the ASME 134 (7).

[21] H. Roy, R. Maiti, Dynamics during speed ratio change of a double roller full toroidal traction drive, in: ASME 2017 International Mechanical Engineering Congress and Exposition, American Society of Mechanical Engineers Digital Collection, 2018.

[22] Q. Li, H. Li, D. Yu, J. Yao, A novel continuously variable transmission with logarithmic disc generatrix, Mechanism and Machine Theory 93 (2015) 147–162.

[23] M. Delkhosh, M. S. Foumani, M. Boroushaki, M. Ekhtiari, M. Dehghani, Geometrical optimization of half toroidal continuously variable transmission using particle swarm optimization, Scientia Iranica 18 (5) (2011) 1126 – 1132.

[24] A. Afrabandpey, H. Ghariblu, Performance evaluation of ball cvt and comparison with half toroidal cvt, International Journal of Automotive Technology 19 (3) (2018) 547–557.

[25] J. Carter, D. Miller, The design and analysis of an alternative traction drive cvt, Tech. rep., SAE Technical Paper (2003).

[26] G. McIndoe, J. VanSelous, T. Liu, J. David, Efficiency analysis of multi-mode passenger car transmission concepts featuring a variglide® cvt, Tech. rep., SAE Technical Paper (2016).

[27] D. C. Miller, Continuously variable transmission, uS Patent 7,074,154 (Jul. 11 2006).

[28] D. C. Miller, D. J. Allen, R. A. Smithson, J. A. Birchak, Continuously variable planetary gear set, uS Patent 7,217,215 (May 15 2007).

[29] D. C. Miller, D. J. Allen, R. A. Smithson, Continuously variable planetary gear set, uS Patent 7,198,584 (Apr. 3 2007).

[30] R. Smithson, D. Miller, D. Allen, Scalability for an alternative rolling traction cvt, Tech. rep., SAE Technical Paper (2004).

[31] Q. Li, X. Zhou, S. Wang, J. Liang, Power split transmission with continuously variable planetary ratio, Mechanism and Machine Theory 140 (2019) 765–780.

[32] R. Alò, F. Bottiglione, G. Mantriota, An innovative design of artificial knee joint actuator with energy recovery capabilities, Journal of Mechanisms and Robotics 8 (1) (2016) 011009.

[33] E. Mobedi, M. İ. C. Dede, Geometrical analysis of a continuously variable transmission system designed for human-robot interfaces, Mechanism and Machine Theory 140 (2019) 567–585.

[34] C. Everarts, B. Dehez, R. Ronsse, Novel infinitely variable transmission allowing efficient transmission ratio variations at rest, in: 2015 IEEE/RSJ International Conference on Intelligent Robots and Systems (IROS), IEEE, 2015, pp. 5844–5849.

[35] C. Everarts, B. Dehez, R. Ronsse, Continuously variable planetary transmission, uS Patent App. 15/308,830 (Mar. 23 2017).

[36] S. Chen, L. Xu, H. Xu, J. Liu, G. Cheng, K. Cao, Principle, design and simulation of a novel continuously variable transmission for robots, in: 2019 IEEE 8th Joint International Information Technology and Artificial Intelligence Conference (ITAIC), IEEE, 2019, pp. 73–78.

[37] M. Tomaselli, P. Lino, G. Carbone, Modelling and efficiency formulation of a planetary traction drive cvt, IFAC-

PapersOnLine 52 (5) (2019) 411–416.
[38] S. Maldotti, Sulla energia dissipata in alcuni organi di macchina, Ph.D. thesis, Alma Mater Studiorum (2009).
[39] S. G. T. Documentation, Quaderni di formazione: i cuscinetti volventi,, Tech. rep., RIV-SKF industrie s.p.a., Torino, Italy (1983).
[40] B. J. Hamrock, Fundamentals of Fluid Film Lubrication (The McGraw-Hill series in mechanical engineering), McGraw-Hill, 1994.